Proceedings of the Combustion Institute

Effects of detailed geometry and real fluid thermodynamics on Spray G atomization

--Manuscript Draft--

Manuscript Number:	
Article Type:	6. Spray/Droplet/Supercritical Combust.
Keywords:	spray atomization; computed tomography; homogeneous equilibrium model; string cavitation; drop sizes.
Corresponding Author:	Marco Arienti Sandia National Laboratories UNITED STATES
First Author:	Marco Arienti
Order of Authors:	Marco Arienti
	Brandon A Sforzo
	Christopher Powell
Abstract:	We present recent results toward the quantification of spray characteristics at engine conditions for an eight-hole counter-bored (stepped) GDI injector – Spray G in the ECN denomination. Two novel elements are presented in the framework of sharp-interface reconstruction of the fuel surface: the detailed description via tomography reconstruction of an actual injector's internal surfaces; and a general equation of state that represents the thermodynamic properties of homogenous liquid-vapor mixtures. The combined level-set moment-of-fluid (CLSMOF) approach, coupled to an embedded boundary formulation for moving solid walls, makes it possible to seamlessly connect the injector's internal flow to the spray. The Large Eddy Simulation (LES) discussed here presents evidence of partial hydraulic flipping and, during the needle's closing transient, string cavitation. Results are validated by measurements of spray density profiles and droplet size distribution.

Effects of detailed geometry and real fluid thermodynamics on Spray G atomization

Marco Arienti[a],

Brandon Sforzo[b], Chris Powell[b]

[a] Sandia National Laboratories, Livermore, CA 94551-0969, USA

[b] Argonne National Laboratory, Lemont, IL 60439-4854 USA

Session: SPRAY, DROPLET, AND SUPERCRITICAL COMBUSTION

Total Length of Paper: 5765 words

Itemization:

Figures + Captions
Figure (1) = 182.6+55
Figure (2) = 72.6+50
Figure (3) = 134.2+31
Figure (4) = 237.6+76
Figure (5) = 129.8+28
Figure (6) = 462+75
Figure (7) = 268.4+25
Total = 1487+337 = 1824 words

Tables = 0 words

Equations = 127 words

References = 385 words

Main text = 3429 words

Effects of detailed geometry and real fluid thermodynamics on Spray G atomization

Marco Arienti[a],

Brandon Sforzo[b], Chris Powell[b]

[a] Sandia National Laboratories, Livermore, CA 94551-0969, USA

[b] Argonne National Laboratory, Lemont, IL 60439-4854 USA

Abstract

We present recent results toward the quantification of spray characteristics at engine conditions for an eight-hole counter-bored (stepped) GDI injector – Spray G in the ECN denomination. Two novel elements are presented in the framework of sharp-interface reconstruction of the fuel surface: the detailed description via tomography reconstruction of an actual injector's internal surfaces; and a general equation of state that represents the thermodynamic properties of homogenous liquid-vapor mixtures. The combined level-set moment-of-fluid (CLSMOF) approach, coupled to an embedded boundary formulation for moving solid walls, makes it possible to seamlessly connect the injector's internal flow to the spray. The Large Eddy Simulation (LES) discussed here presents evidence of partial hydraulic flipping and, during the needle's closing transient, string cavitation. Results are validated by measurements of spray density profiles and droplet size distribution.

Keywords: spray atomization; computed tomography; homogeneous equilibrium model; string cavitation; drop sizes**.**

1. Introduction

Predicting the primary atomization properties of fuel blendstocks is essential for understanding fuel performance in advanced combustion engines. Properties such as density, viscosity, surface tension, boiling point and heat of vaporization change the way that fuel mixes with air in an engine. The resulting fuel distribution affects ignition, burn-rate, particulate matter, and knock sites — all key parameters that directly impact efficiency.

This study is limited to non-flashing conditions, but includes the transient flow associated with needle closing. For flashing conditions, the reader is referred to recent work in [1] and references therein. Previous experimental studies on multi-hole sprays at non flash-boiling conditions, such as [2], indicate that sprays with similar magnitudes of Weber number, Reynolds number and air-to-liquid density ratio have similar structure and characteristics. These observations often do not take into account the details of multi-hole design and are limited to the quasi-stationary phase of injection. In reality, throttling effects during needle opening and closing, when cavitation and gas ingestion become more relevant, are increasingly relevant in injector operation.

Spray G is the eight-orifice stepped-hole valve-covered orifice (SVCO) injector built by Delphi for the Engine Combustion Network (ECN) [3]. The operating liquid is iso-octane. The full angle between orifices is 80^{o}, with the counterbore machined coaxially with each of the eight inner holes. The length-to-diameter ratio of the nozzle holes and counterbores are approximately 1 and 1.2, respectively, and their nominal diameters are 165 µm and 388 µm. A novel element in our study is that nominal geometry specifications are not used to generate the computational mesh: wall surfaces are instead built from the reconstructed 3-D volume of an existing injector hardware (specimen #28) from X-ray computed tomography (CT) to capture real geometry effects on spray formation.

The second element of interest in this paper is the use of a sharp-interface method to separate a fuel vapor-liquid homogenized mixture from the non-condensable (NC) gas phase. This approach enables a straightforward thermodynamic description of blended fuels, whose study is the ultimate objective of our project. In homogenized form, vapor bubbles are not individually resolved and therefore the effects of surface tension are ignored. It is also assumed that the response of the liquid-vapor composition to a change of thermodynamic state is instantaneous, following the Homogenous Equilibrium Model (HEM) as described, for instance, in [4]. HEM is considered appropriate for bubbly flows when interphase momentum exchange is fast and large enough to prevent slip between the two phases.

A homogenous equilibrium barotropic model coupled to volume of fluid (VOF) interface reconstruction was proposed in [5] to study cavitation over a sharp corner. As the flow was assumed to be isentropic, the solution of the energy equation was not required. In [6], the energy equation was included in the description of the three-phase (liquid, vapor, and air) system for the study of a more relevant multi-hole injector geometry, but with a diffuse interface approach. A modified multiphase mixture energy equation, including the enthalpy of phase change due to cavitation, was integrated with sharp-interface VOF reconstruction in [7]. In a similar framework, Biçer and Sou [8] proposed an improved interfacial mass transfer model between the liquid and the vapor phase. A combination of similar techniques is found in the study of hydraulic flipping and cavitation by Bode et al. [9].

In the approach presented here, we build on previous work [10] to separate the non-condensable gas (Material 2) from a vapor-liquid mixture that is locally at equilibrium (Material 1). Material 3 in the simulation is the injector itself, which is included by the embedded boundary approach described in [11]: the needle is allowed to rigidly move with respect to the injector following the measured

trajectory during opening and closing operations. The description of key elements of the representation of a real gasoline injector and of a general equation of state is presented next; the equations governing the motion of multiphase, compressible flow and the implementation details can be found in the included references. The rest of the paper is dedicated to the analysis of simulation results for the fully unseated needle position, where validation data are available, and for an intermediate position during the closing transient.

2. Implementation

2.1. Real geometry representation

The surface geometry was obtained from the composition of two distinct scans. The whole injector was initially scanned by a commercial X-ray source with voxel resolution of 5 μm [12]. After the signal was imaged by a digital detector array, the two-dimensional transmission maps obtained from different angles were inverted and combined into a 3-D tomographic reconstruction. The cross-section in Figure 1 illustrates the overall injector geometry and its location within the computational domain. A second scan was then carried out to characterize the internal geometry of the orifices and counter-bores with a resolution of 2 μm (Figure 2a). For the discussion that follows it is important to point out that, while the eight holes exhibit fairly similar shape from inner orifice inlet to step-hole outlet, they are slightly different in taper [13]; in Figure 2b, the example of two super-imposed axial cross-sections of the injector shows that orifice 7 (continuous line) has almost no taper and a slightly sharper radius of curvature compared to orifice 5 (dashed line). The reader is referred to Figure 4 for the hole numbering order.

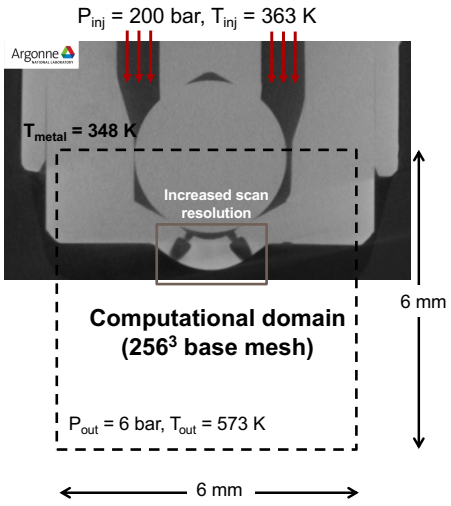

Figure 1. Placement of the computational domain with respect to the injector. The domain boundaries are indicated by the dashed lines. The background picture is the cross-section of the injector's X-ray tomography with voxel resolution of 5 µm. The rectangular inset corresponds to the higher resolution tomography of the orifices' inner walls, see Figure 2.

.

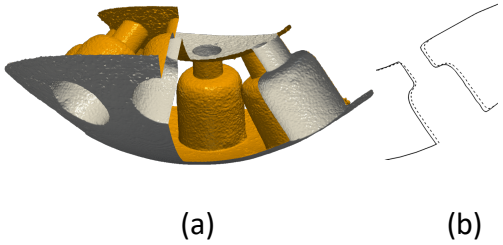

Figure 2. (a) Partial section view of the ECN Spray G #28 isosurface, as generated from X-ray computed tomography (CT). The rendered region has a spatial resolution of 2 µm. (b) Superposition of axial cross-sections passing through hole 5 (dashed line) and hole 7 (continuous line) and rotated to overlap.

2.2. Computational approach

Following the Moment of Fluid Method [14], the piecewise-linear reconstruction of the gas-liquid interface is obtained from the location of the phase centroid of the computational cell in addition to the local values of level set (LS) function and volume of fluid (VOF). This approach corrects the drawback of VOF-style methods that require non-local data to determine the orientation of the interface. The multi-phase compressible Navier-Stokes equations are solved with the directionally-split, Cell Integrated Semi-Lagrangian advection algorithm of Jemison et al. [14]. The solution is advanced in time by a semi-implicit pressure update scheme that asymptotically preserves the standard incompressible pressure projection in the limit of infinite sound speed [15].

As in [10], the wall boundaries of the injector are represented by an embedded boundary method. The method uses a signed distance function, the "solid" LS, whose magnitude is the minimal distance between the cell center and the surface of the body. The evaluation of the boundary normal from the level set function avoids staircase-like artifacts in the solution. The procedures for populating center and face values in the solid ghost region are described in [11]. When applied to moving solid surfaces, such as during the unseating of the injector's needle, the embedded boundary sweeps the computational Cartesian cells: contact and separation of wall surfaces are handled in a straightforward and robust manner as logical operations on level set function values.

The set of compressible Navier-Stokes equations is discretized on blocks of regular Cartesian cells with adaptive mesh refinement (AMR) to concentrate the computational resources at the liquid surface. AMR and data allocation in CLSVOF are managed by the library AMRex (https://amrex-codes.github.io/). The Cartesian blocks are distributed amongst processes according to common load-balancing strategies such as knapsack and space-filling curve.

Finally, the calculation in executed in the framework of a highly resolved LES. Because of its suitability to wall-bounded flows, the turbulent viscosity μ_t follows the wall-adapting local eddy-viscosity model (WALE) [16], but no sub-grid term is added to the liquid surface.

2.3. Liquid-vapor equation of state for fuels

The density-based formulation of the solver requires the retrieval of the equilibrium vapor quality given the cell density ρ_{eq} and internal energy ie_{eq}. The first step in solving this problem is the comparison of the input ρ_{eq} with the saturation density along the isotherm at equilibrium temperature T_{eq}. Let us first assume the T_{eq} is known; then, If $\rho_{eq} < \rho_{s,L}(T_{eq})$, a smaller ρ_{eq} can only be accounted for by a finite volume occupied by vapor. Accordingly, the vapor quality is evaluated as

$$q_{eq} = \frac{\frac{1}{\rho_{s,L}} - \frac{1}{\rho_{eq}}}{\frac{1}{\rho_{s,L}} - \frac{1}{\rho_{s,V}}} \tag{1}$$

The solution is more involved when ie_{eq} is known instead. If there is only liquid phase, the solution is found by inverting the relation

$$ie_L(T) = ie_{eq}, \tag{2}$$

where, for simplicity, the dependence of internal energy on pressure is dropped. If the vapor quality is finite, the definition of internal energy of vaporization, $eov = ie_{s,L} - ie_{s,V}$, dictates the equation

$$ie_{s,L}(T) + eov(T) \cdot q(T, \rho_{eq}) = ie_{eq}. \tag{3}$$

Looking at the density-energy diagram, Figure 3, one recovers the result that for the same internal energy the temperature of the liquid phase is always greater than the temperature of the liquid-vapor mixture. To pick the correct T_{eq} out of the many possible values that correspond to ie_{eq}, however, the input value ρ_{eq} needs to be accounted for in an iterative manner.

The general solution algorithm is started by solving Eq.(2) to find T_L and by assigning the initial guess $T' = T_L$. Then:

1. Evaluate the running internal energy of the mixture based on Eqn. (1):

   $ie' = ie_{s,L}(T') + eov(T') \cdot q(T', \rho_{eq})$;

2. If $\left|ie'/ie_{eq} - 1\right|$ is less than an assigned threshold, then $T_{eq} = T'$; exit from the loop;
3. Recalculate the liquid phase temperature in Eq. (2) with the new ie' and find $T_L{}'$;
4. The new tentative temperature is $T' = T' - (T_L' - T_L)$. Repeat the loop.

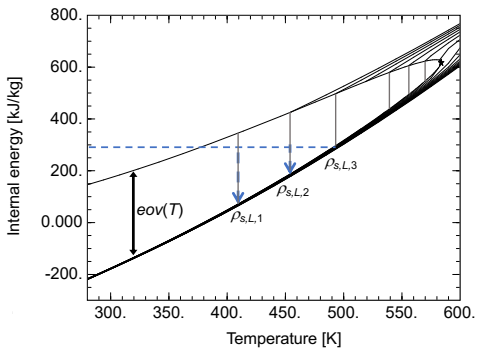

Figure 3. Saturation curve in the internal energy-temperature diagram. The sequence of saturation density values, $\rho_{s,L,1}$, $\rho_{s,L,2}$, $\rho_{s,L,3}$ can be considered as successive approximations of the solution identified by the dashed line.

The required thermo-physical properties for both pure liquid and vapor-liquid mixture are obtained from the NIST REFPROP (Reference Fluid Thermodynamic and Transport Properties Database) version

10 [17]. REFPROP incorporates high-accuracy Helmholtz equations of state and mixing rules for multicomponent fluids using estimated interaction parameters. The subroutines and the database of the FORTRAN REFPROP program can be directly accessed by the simulation code.

2.4. Computational setup

According to the orientation convention established by the ECN, the positive Z-axis corresponds to the injector axis, the positive X-axis is oriented toward the electrical connector, and the Y-axis is located into the page based on the right hand rule convention. The origin of the coordinate system is at the end of the nozzle tip.

The experimental conditions set for Spray G at ECN conditions are ambient temperature of 573 K, ambient density of 3.5 kg/m^3 (at approximately $6 \cdot 10^5$ Pa) and nominal injection pressure of $2 \cdot 10^7$ Pa. The electronic injection duration was set to 680 μs. The needle displacement at fully open condition, reached between 0.1 and 0.6 ms after start of injection (aSOI), was measured at 52 μm. To contrast the pseudo-steady condition at fully open conditions, we also consider a point during the closing transient, at time t = 0.74 ms aSOI, when the lift is reduced to 23.5 μm.

The computational domain is a 6 x 6 x 6 mm cube centered at the injector's tip. The base block is a 256^3 cell Cartesian box, which is further subdivided in 16^3 blocks to facilitate load balancing. Three more levels of refinement were added during the simulation, reaching the final grid resolution of Δx = 2.93 μm. The resulting cell count was approximately 450 million when the third level of refinement only included the sac volume, the orifices and the counterbores of the injector; it then grew to 800 million when the third level of refinement included one of the plumes, for grid convergence assessment.

Calculations were carried out at Sandia National Laboratories on the HPC Production Linux Clusters: Sky Bridge and Chama (Cray 2.6 GHz Intel Sandy Bridge 16 cores/node, InfiniBand interconnect); and Ghost (2.1 GHz Intel Broadwell 36 cores/node, Omni-Path interconnect).

3. Numerical results

Two representative injector's states are investigated in this preliminary study. The first corresponds to approximately 0.3 ms from the needle's activation, which corresponds to a fully open needle, quasi-stationary injection phase. At these conditions, a fairly large data set is available for validation: the measured mass flow rate is 14.0±0.4 g/s [18] and density radiography scan were taken in the near-orifice region. The second condition is near the end of injection, where cavitation effects are expected.

3.1. Internal flow

Expansion driven by the large pressure differential and internal friction affect the fuel state at the injector's exit. In particular, the fuel exit temperature depends on two opposite processes: viscous heating, when the fuel is forced to pass through the gap between the needle and the inner injector wall; and expansion cooling [10]. The fuel density decreases from 660 kg/s at the inlet $2 \cdot 10^7$ Pa to a cross-sectionally averaged value of 626 kg/s at the orifice exit, but the temperature remains close to the inlet value.

The mass flow rate is evaluated by integrating the product of density (in the liquid phase only) by the velocity normal to the hole cross-section. At fully unseated needle, the time-average from six snapshots between 0.291 and 0.296 ms is $\dot{m}$ = 14.4±1.1 g/s, corresponding to the discharge coefficient C_d = 0.54. This result is very close to the coefficient reported by Payri et al. [19].

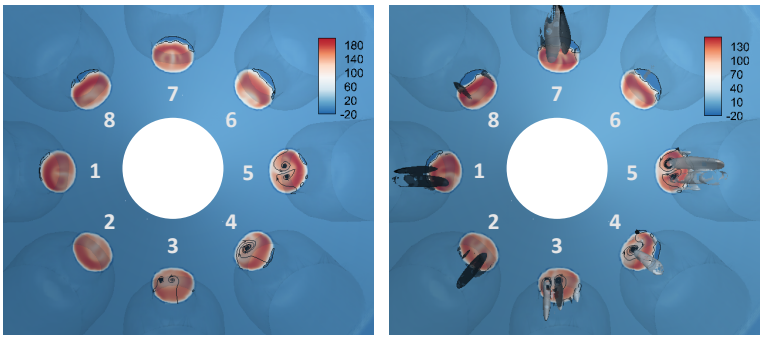

(a) (b)

Figure 4. Flow velocity (in m/s) projected in the hole axial direction (normal velocity) at full opening (a) and during the closing transient (b). A truncated conical surface cuts perpendicularly through the eight holes and is used to display their cross-sections. Areas occupied by the gas within the holes are delimited by a line and indicate hydraulic flipping. Streamlines are drawn to characterize vorticity distribution. In frame (b), iso-surfaces at q = 0.001 are also shown.

Closer examination of the injector's orifices reveals hydraulic flipping in some of the holes but not in others. Out of the eight cross-sections shown in Figure 4, portions of the holes are occupied by non-condensable gas even at fully unseated needle. In frame (a), hydraulic flipping does not occur in holes 2 and 3, while it is quite visible in the opposite holes 6, 7, and 8. During needle closing (in frame (b)) the replacement of liquid by external gas is more evident, but it is still not uniform across all the holes. The cause of this irregular behavior can be explained by the fact that some of the holes have slightly positive taper while others have neutral or even slightly negative taper, as shown by Figure 2b. In addition, the geometry of the sac is not perfectly axis-symmetric, therefore placing of the needle ball favors certain fuel passages and not others.

Vortices are generated near the orifice entry because of the strong adverse pressure gradient encountered by the fuel entering the nozzle sac, similarly to what observed in [1] at flash boiling. The existence of vortical structures, suggested by the contour plot of the hole axial velocity projection in Figure 4, is further evidenced by drawing a few streamlines at the holes' cross-sections. Hole vortices appear in various forms and strength, for instance holes 1 and 3 host pairs of counter-rotating vortices whereas hole 2 seems to contain a single main vortex.

At end of injection, these stronger vortices tend to embed cavitation strings, shown in frame (b) as iso-surfaces of vapor quality at q = 0.001. Perhaps the most interesting observation here is that there are holes that are affected by both string cavitation and hydraulic flipping, and others that exhibit only one or the other of these phenomena. In Figure 4 the iso-surfaces end within the volume of the counter-bore, as expected because of the assigned back pressure (lower back pressures would allow the vapor core to continue expansion outside of the injector reaching flash-boiling conditions). Hydraulic flipping becomes more critical: in the final phase of the needle closure liquid fuel continues exiting the orifice, mostly in the form of dribble, while outside gas moves in to fill the sac.

3.2. External flow

A snapshot of the spray at fully open conditions is shown in Figure 5. Evidence of liquid splashing on the counterbore surfaces can be found at several locations; droplets depositing there reach high surface temperatures. Outside of the injector, the spray fuel density decreases because of heat transfer.

Since the velocity distribution at the orifices is unequal, the liquid jets are not aligned with the counterbore axes nor are they circular in cross-section. The jets tend to deform into curved, elongated

sheets that can even fold on themselves, as illustrated by Figure 5: it is only in a time-averaged sense that their cross-sections can appear circular. The jets rapidly disintegrate due to the strong turbulent flow caused by gas entrainment, although at the outer boundary of the computational domain (at 2.2 mm from the injector's tip) the primary atomization process is still incomplete.

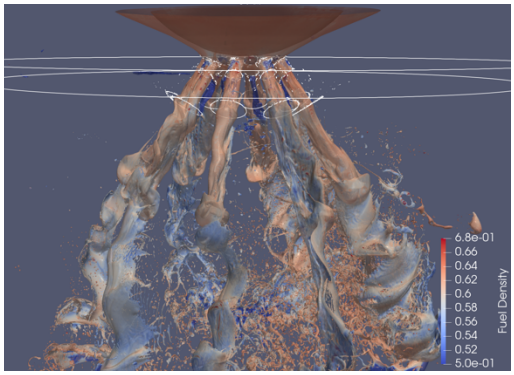

Figure 5. Spray G snapshot: the zero level rendering is colored by the density of the mixed phase. Only the edges of the injector are shown for clarity.

The spray angle can be assessed from the prevalent fuel radial mass distribution. This can be obtained by averaging the plume densities along four planes cut through the geometrical axis of the injector and rotated by increments of 45°. The traces of these planes are shown as dashed lines in the top left picture of Figure 6.

The Argonne's X-ray density measurement displayed here comes with two caveats: the operating liquid used for the Z = 2 mm was Viscor 16BR, injected at $1.9 \cdot 10^7$ Pa and 25°C, instead of iso-octane; and the ambient gas in the facility could only be heated up to 45°C for cross-section Z = 1 mm, corresponding to a density of approximately 6 kg/m^3. To obtain the Z = 2 mm cross-section, the ambient gas was set

at 25°C but at a lower pressure, $3.15 \cdot 10^5$ Pa, to reach a density closer to the ECN-prescribed value of 3.5 kg/m^3. Overall, the simulation results agree with the measured fuel mass distribution, particularly at Z = 2 mm. It is noted that the density value in the inner part of the plume is not zero, as many droplets recirculate in the interior part of the spray.

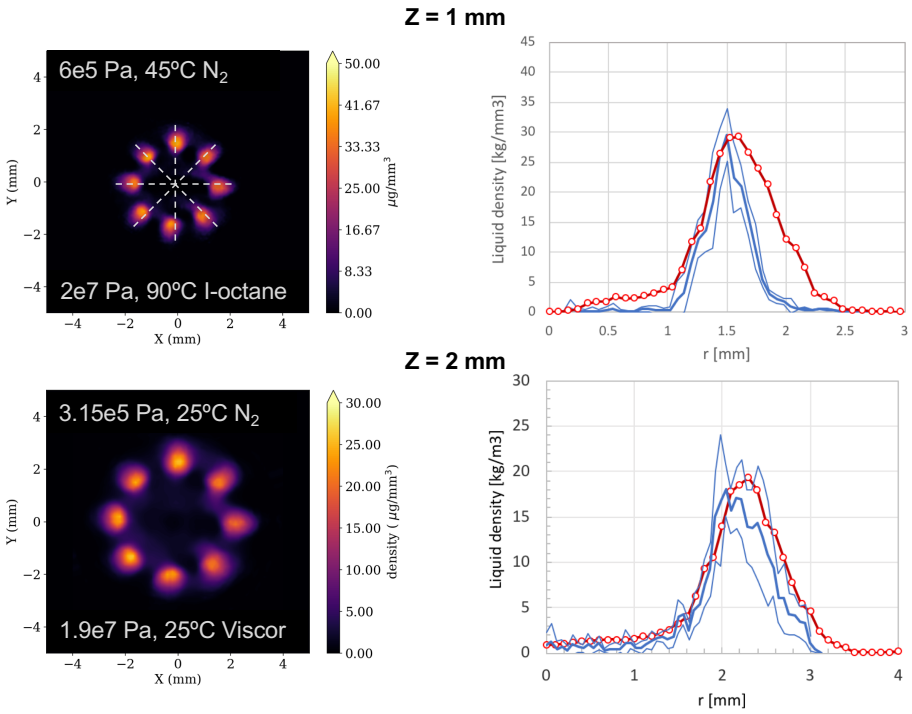

Figure 6. Left: Cross-sectional density scan from X-radiography at 1 mm and 2 mm from the tip of the injector, time-averaged between 0.6 and 0.8 ms after SOI. Right: plot of density along the directions marked by the dashed line. Symbols correspond to the density scan, the continuous lines are obtained by time average of snapshots of the simulation (the thinner lines correspond to the average plus and minus the standard deviation).

3.3. Droplet size distribution

To post-process simulation data and extract droplet characteristics, the zero iso-surface of the level set function is transformed into polyhedra made of triangular and quadrilateral faces. For simplicity, we

focus on fully formed droplets smaller than 100 μm; this is a convenient cut-off length since detached ligaments and membranes that coexist with the droplets are consistently larger. In this analysis, the exclusion of polyhedra with less than 16 faces ensures that extreme cases of under-resolved liquid structures are discarded.

From the volume and the surface area of each polyhedron, V and S, the diameters of the volume-equivalent and surface-equivalent sphere are

$$D_V = \left(\frac{6V}{\pi}\right)^{1/3}, \qquad D_S = \left(\frac{S}{\pi}\right)^{1/2}. \tag{4}$$

For a collection of N droplets with $\{D_{V,i}\}$, $\{D_{S,i}\}$, i=1..N, the Sauter Mean Diameter is

$$\mathrm{SMD} = \frac{\sum_i D_{V,i}^3}{\sum_i D_{S,i}^2} = 6\frac{\sum_i V_i}{\sum_i S_i}. \tag{5}$$

Additional analysis, particularly on derivation of droplet shape distribution, is presented in [10].

The histograms of Figure 7 show two representative distributions of D_V when the fuel passages are fully open. The left plot includes the spray droplets from the eight plumes at grid resolution of Δx = 5.86 μm, forming a total sample population of 33,813 droplets from four snapshots within a 3 μs interval; the right plot includes 6334 droplets from only one of the plumes, between Z = 0.22 mm and Z = 0.32 mm, where an additional level of refinement was added to reach Δx = 2.93 μm in the spirit of a grid refinement study. Both distributions indicate that the size interval of fully formed droplets is rather narrow and has a peak frequency at approximately 10 μm. However, the SMD value according to Eqn. (5) is 30 μm for the coarser grid resolution and 19 μm for the finer grid. This disparity reflects the shift in Figure 7 toward smaller droplets thanks to increased grid resolution.

The SMD value of 19 μm is comparable with the Phase Doppler Interferometry measurements reported in a study by General Motors (courtesy of Scott Parrish) at ECN 4 [20]. The measurements

were taken between 0.2 and 1.5 ms after SOI across the plume at Z = 15 mm in a region extending 9 mm radially and 6 mm tangentially. In most of this region the droplet count was above 300 and the SMD distribution was relatively uniform in the range 9-13 μm.

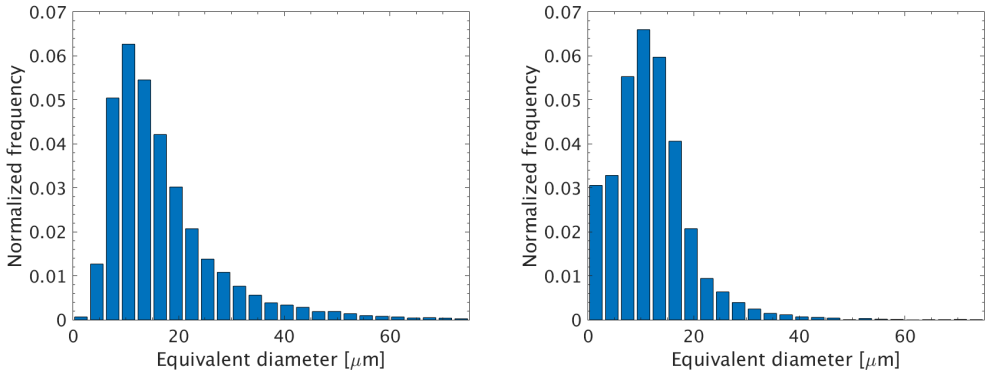

Figure 7. Histograms of the droplets' equivalent diameter. Left: effective grid spacing Δx = 5.86 μm – all eight plumes. Right: Δx = 2.93 μm – single plume.

4. Conclusions

The role of the injector's geometry in developing the complex spray configuration and plume interaction of Spray G has been investigated in this work. The computational framework is sufficiently flexible and comprehensive that no calibration tuning or model switching is required. In this way we are able to show that string cavitation and hydraulic flipping may occur at the same time during the injection closing transient. The availability of near-field droplet size distribution is also an important result for the transition to a spray Lagrangian model that could enable ignition and combustion simulations at engine scale. Finally, the availability of a thermodynamic database for fuel blends is relevant to the comparison of spray characteristics with respect to the iso-octane baseline. Target blendstock fuels are oxygenated blending (BOBs) which are intended to meet the gasoline

requirements for octane number, vapor pressure, and other properties after ethanol has been added to them. Those simulations are ongoing.

5. Acknowledgments

We gratefully acknowledge funding from the Co-Optima program by the U.S. DOE Vehicle Technologies Program.

Sandia National Laboratories is a multi-mission laboratory managed and operated by National Technology and Engineering Solutions for Sandia LLC, a wholly owned subsidiary of Honeywell International, Inc., for the U.S. Department of Energy's National Nuclear Security Administration under contract DE-NA0003525.

6. References

1. E.T. Baldwin, R.O. Grover Jr, S.E. Parrish, D.J. Duke, et al., String flash-boiling in gasoline direct injection simulations with transient needle motion. International Journal of Multiphase Flow 87 (2016) 90-101.

2. W. Zeng, M. Xu, M. Zhang, Y. Zhang, D.J. Cleary, Macroscopic characteristics for direct-injection multi-hole sprays using dimensionless analysis, Exp. Therm. Fluid Sci. 40 (2012) 81-92.

3. Engine Combustion Network, ECN Spray G, 2016 available at https://ecn.sandia.gov/gasoline-spray-combustion/target-condition/spray-g-operating-condition/

4. D.P. Schmidt, C.J. Rutland, M.L. Corradini, A fully compressible two-dimensional model of small, high speed cavitating nozzles. Atomization and Sprays 9 (1999) 255-276.

5. M.G. Mithun, P. Koukouvinis, M. Gavaises, M., Numerical simulation of cavitation and atomization using a fully compressible three-phase model. Physical Review Fluids, 3(6), 064304 (2018).

6. R. Torelli, S. Som, Y., Pei, Y. Zhang, et al., Comparison of In-Nozzle Flow Characteristics of Naphtha and N-Dodecane Fuels, SAE Technical Paper 2017-01-0853 (2017).

7. Yu, H., L. Goldsworthy, P.A. Brandner, V. Garaniya, Development of a compressible multiphase cavitation approach for diesel spray modelling, Applied Mathematical Modelling, *45* (2017) 705-727.

8. B. Biçer, S. Akira "Application of the improved cavitation model to turbulent cavitating flow in fuel injector nozzle." Applied Mathematical Modelling 40, 7-8 (2016) 4712-4726.

9. M. Bode, T. Falkenstein, M. Davidovic, H., Pitsch, et al., Effects of cavitation and hydraulic flip in 3-hole GDI injectors. SAE International Journal of Fuels and Lubricants, *10*(2), (2017) 380-393.

10. M. Arienti, M. Sussman. A numerical study of the thermal transient in high-pressure Diesel injection. Int. Journal of Multiphase Flow 88 (2017) 205-221.

11. M. Arienti, M. Sussman, An Embedded Level Set Method for Sharp-Interface Multiphase Simulations of Diesel Injectors. Int. J. of Multiphase Flow 59 (2014) 1-14.

12. J. Manin, Y. Jung, S.A. Skeen, L.M. Pickett, S.E. Parrish, L.E. Markle, Experimental Characterization of DI Gasoline Injection Processes, SAE Technical Paper 2015-01-1894 (2015).

13. P. Strek, D. Duke, A. Swantek, A. Kastengren, C.F. Powell, D.P. Schmidt, X-Ray Radiography and CFD Studies of the Spray G Injector, SAE Technical Paper 2016-01-0858 (2016).

14. M. Jemison, E., Loch, M. Sussman, M. Shashkov, M. Arienti, et al., Coupled Level Set-Moment of Fluid Method for Incompressible Two-Phase Flows. J. Sci. Comput. 54(2-3) (2013) 454-491.

15. M. Jemison, M. Sussman, M. Arienti, Compressible, Multiphase Semi-Implicit Method with Moment of Fluid Interface Representation. J. Comput. Phys., 279, (2014) 182-217.

16. F. Nicoud, F. Ducros, Subgrid-scale stress modelling based on the square of the velocity gradient tensor. Flow, Turbulence and Combustion, 62(3), (1999) 183-200.

17. E.E. Lemmon, M.L. Huber, M.O. McLinden, NIST standard reference database 23. NIST reference fluid thermodynamic and transport properties-REFPROP, Version 9, 55 (2010).

18. R. Payri, J. Gimeno, P. Martí-Aldaraví, D. Vaquerizo, Internal flow characterization on an ECN GDi injector, Atom. Sprays 26 (9) (2015) 889-919.

19. R.Payri, F.J. Salvador, P. Martí-Aldaraví, D.Vaquerizo, ECN Spray G external spray visualization and spray collapse description through penetration and morphology analysis, Applied Thermal Engineering 112 (2017) 304-316.

20. Engine Combustion Network, ECN4 Proceedings 2014 available at https://ecn.sandia.gov/ecn-workshop/ecn4-workshop/

Figure 1. Placement of the computational domain with respect to the injector. The domain boundaries are indicated by the dashed lines. The background picture is the cross-section of the injector's X-ray tomography with voxel resolution of 5 μm. The rectangular inset corresponds to the higher resolution tomography of the orifices' inner walls, see Figure 2.

Figure 2. (a) Partial section view of the ECN Spray G #28 isosurface, as generated from X-ray computed tomography (CT). The rendered region has a spatial resolution of 2 μm. (b) Superposition of axial cross-sections passing through hole 5 (dashed line) and hole 7 (continuous line) and rotated to overlap.

Figure 3. Saturation curve in the internal energy-temperature diagram. The sequence of saturation density values, $\rho_{s,L,1}$, $\rho_{s,L,2}$, $\rho_{s,L,3}$ can be considered as successive approximations of the solution identified by the dashed line.

Figure 4. Flow velocity (in m/s) projected in the hole axial direction (normal velocity) at full opening (a) and during the closing transient (b). A truncated conical surface cuts perpendicularly through the eight holes and is used to display their cross-sections. Areas occupied by the gas within the holes are delimited by a line and indicate hydraulic flipping. Streamlines are drawn to characterize vorticity distribution. In frame (b), iso-surfaces at q = 0.001 are also shown.

Figure 5. Spray G snapshot: the zero level rendering is colored by the density of the mixed phase. Only the edges of the injector are shown for clarity.

Figure 6. Left: Cross-sectional density scan from X-radiography at 1 mm and 2 mm from the tip of the injector, time-averaged between 0.6 and 0.8 ms after SOI. Right: plot of density along the directions marked by the dashed line. Symbols correspond to the density scan, the continuous lines are obtained by time average of snapshots of the simulation (the thinner lines correspond to the average plus and minus the standard deviation).

Figure 7. Histograms of the droplets' equivalent diameter. Left: effective grid spacing $\Delta x = 5.86\ \mu m$ – all eight plumes. Right: $\Delta x = 2.93\ \mu m$ – single plume.

declaration of competing interest